

Shoemaker-Levy 9: Distribution of Radiant Energy

Terry Z. Martin

Glenn S. Orton

T.Z. Martin and G.S. Orton are at Jet Propulsion Laboratory,
Mail Stop 169-237,
4800 Oak Grove Drive,
California Institute of Technology,
Pasadena CA 91109 USA

tmartin@jplds.jpl.nasa.gov

go@orton.jpl.nasa.gov

Submitted to *Planetary and Space Science*, November 1996

Revised March 1997

Abstract

Multicolor Galileo observations of several SL9 impacts permit derivation of size and temperature information for the fireball phase. Integration of light curves yields total fireball radiant energy estimates. Event Q 1 has an initial color temperature of 24000 K. Total radiant fireball energy for G was 8.3×10^{24} ergs. The largest event, L, is estimated to be 10^{25} ergs. Modelling of total energy radiated during the fallback phase shows a much larger energy release during that period - up to 4×10^{26} ergs for L. The mass required to provide the equivalent kinetic energy is about 1×10^{13} gm, which is a strong lower limit to initial fragment mass. The fallback energy derived for the R impact is 1×10^{25} erg, with the strongest spectral constraints. Fallback energies for H and Q1 are about 4×10^{25} erg, derived from only two spectral points. The fallback energies extrapolated from the 2.3- μ m lightcurves of the G and K impacts are 7×10^{25} and 9×10^{25} erg, respectively. Uncertainties of the fallback energies are up to an order of magnitude. Improvements to these estimates and their uncertainties will derive from the application of more detailed physical models.

introduction

The kinetic energy transported into the atmosphere of Jupiter by the fragments of Shoemaker-Levy 9 during their impacts is transferred into several different forms. Among these are temperature changes of the atmosphere, various types of waves, radiation escaping from the impact events, and the kinetic energy of the material involved with the upwelling plume and rising fireball. With the re-entry of the latter into the atmosphere, there is further acoustic and radiative escape of energy, as well as heating of the Jovian stratosphere.

The purpose of this review is to determine reasonable bounds to the radiative energy observed from the impacts, which can then serve as a minimum estimate of the energy of the incoming fragment, as well as serve as a boundary condition for detailed physical models. The information determined by this study becomes a useful means to elucidate more information about the impact events. For example, we make a first-order estimate of the effective radiating temperature at different times during the impact phenomena.

For the purpose of this review, our approach will be to examine Galileo remote sensing data for a means of estimating the total radiative energy output from the bolide and fireball phases of the impact events, using terminology adopted during the last Shoemaker-Levy 9 conference (cf. Chapman 1995, Nicholson 1995) and used widely in the SL9 literature. We then examine the suite of available ground-based observations of the subsequent fall-back phase or "main event" to estimate the considerable energy released during that phase. We purposely review only events also observed by Galileo in order to provide a focus for this review and also to attempt to establish a relationships between the observed phenomena.

Fireball Phase

The initial fireball phase of several S1.9 impacts were well observed by the Galileo spacecraft (Martin et al, 1995; Carlson et al, 1995a; Hord et al, 1995; Chapman et al, 1995). We mean by the term “fireball” the hot expansion phase of the entry corridor, as well as any terminal explosion. Although the geometry of the emitting region is complex (Boslough et al, 1995), probably involving a “line charge” that radiates, expands, and cools along its length, we model the emission here for simplicity as that of a spherical blackbody, growing and cooling with time. This model provides a ready means of intercomparing different impact events, as well as assessing total radiant energy.

We focus here on two events, G and Q 1, for which multicolor information is available. G was observed by the Ultraviolet Spectrometer (UVS), Near Infrared Mapping Spectrometer (NIMS), and Photopolarimeter Radiometer (PPR) experiments at wavelengths from 292 nm to 5 μm , with a 5.3 sec sampling interval. Q 1 was observed at 678 and 945 nm by the PPR with a 1.3 sec sampling interval.

The individual measurements have been described elsewhere (Martin et al, 1995; Carlson et al, 1995a; Hord et al, 1995; Chapman et al, 1995). The process of combining the UVS, PPR, and NIMS data involves placing them on a common timeline, in a common physical unit, and then modelling the data available within each of a number of time bins.

The observed radiance at a given wavelength arises not only from the fireball, but from light reflected by underlying clouds. That contribution, which varies with wavelength depending on cloud reflectivity, is subtracted to find the fireball radiance alone. We believe that most of the fireball emission comes from above the clouds based on the modelling by Carlson et al (1995a) of band absorption in the near IR spectrum of the G event. They found a pressure level above about 200 mb for the upper fireball surface, which is above the likely ammonia cloudtop.

The reflection of the cloud is modelled to be $3A_g \cos \theta$, Where A_g is the cloud geometric albedo and θ is the angle of Galileo from the zenith. This equation arises from an integration of the intensity from a spherical fireball seen at the surface of an underlying planar cloud. Values of the albedo (Table 1) were taken from the work of Karkoschka (1994) for wavelengths below 1 μm , and from Carlson (1995b) for the NIMS wavelengths. The albedos are those of the Jovian disk, presumed to apply to the ammonia cloud deck alone.

For each time, an iterative manual process selects a single temperature and blackbody diameter to fit the set of measurements:

$$S_\lambda(t) = \omega(t) B_\lambda(T(t)) \quad (1)$$

where ω is the solid angle represented by the fireball, and B is the Planck function of wavelength and temperature. After doing this fitting for each of the time steps, a second pass is made, using the first pass results as a guide. It is assumed that the temperature declines with time, and the diameter increases. We show in Fig. 1 the collection of radiance values used for G, and in Fig. 2 the resulting model surface $S(t)$ that expresses the changing spectral energy distribution. Note that the model shows a peak radiance occurring in the visible range at about 6 seconds. That is both a wavelength and time not sampled by Galileo.

For Q1, the raw PPR data involve a low signal to noise ratio (Martin et al, 1995). We chose to smooth the data by drawing light curves through the points (Fig. 3), scaling the results of larger events at 945 ntn (Martin et al, 1995) and the peaked behavior of the SS1 data for W (Chapman et al, 1995). In this way, we can extract a relatively well-behaved spectral energy distribution for Q 1, using the same approach as for G. Our coverage of the spectrum is of course much reduced. The peak of the 678 nm curve for Q 1 is clearly much larger than at 945 nm, implying a high color temperature. This determination depends critically on the accuracy of that flux ratio, which is affected by noise and by the calibration of those two channels of the PPR. We believe that, in spite of the noise level apparent in Fig.

3, [he overall curve can be drawn with some accuracy, and that the ratio is unlikely to be in error by more than 25 %. The nominal uncertainty of the ratio is consistent with color temperatures in the range 9500-60000 K. The relative calibration was to have been checked in June 1996 during the first Ganymede encounter, but the PPR suffered a filter wheel anomaly prior to the calibration, leaving the instrument in a radiometric filter position. Such high temperatures and Planck spectral behavior are consistent with the predictions of several researchers for a shocked gas environment (Ahrens, 1994; Chevalier and Sarazin, 1994; Borovicka and Spurny, 1996). We can not rule out, however, the existence of line emission with the meager spectral coverage available.

The resulting temperature and diameter data (Figs. 4, 5) reveal several interesting features. Note that the G data, with lower time resolution, must be time aligned with Q 1 in order to intercompare the two cases. We do not know the time origin as well for G due to the 5 sec sampling. The chosen alignment expresses the feeling that G would likely show greater energy than Q 1 in the first few seconds. In this case, initial G data were not sampled by Galileo, and would have shown even greater radiance in the seconds preceding the first UVS/PPR detection. It seems unlikely that the weaker Q 1 event would have produced color temperatures higher than those found for G.

The temperatures of Q 1 fall faster than those of G, most likely due to more effective radiation through a smaller volume of heated material. The G fireball grows in size faster, consistent with a greater total energy.

We may integrate the area beneath the spectral energy distributions for G and Q 1 to derive an estimate of the total radiated energy in the fireball phase. It is apparent from Fig. 2 that the bulk of the area is in the first 20 seconds of the events. Although we do not sample wavelengths near the blackbody peak for all that time, it is unlikely that the integral is in error by as much as a factor of two. We derive energies of 8.4×10^{24} ergs for G and 3.2×10^{24} ergs for Q1.

The radiant energy we compute here is not necessarily the largest part of that converted from the initial kinetic energy. Indeed, the energy radiated further in the infrared minutes later during the "fallback" phase appears to exceed the initial fireball radiation. The fallback portion of the energy is converted from the kinetic energy of the rising fireball.

Since both G and Q 1 were measured at 945 nm, we may plot their peak flux at that wavelength versus total radiant energy (Fig. 6). This relationship offers a means of characterizing the other impacts for which we obtained 945 nm data, namely H and L (Martin et al, 1995). The H event appears intermediate in intensity, while L is the largest of all, with a total fireball radiant energy of about 1×10^{25} ergs.

The PPR 945-rim lightcurve data represent a unique set of observing circumstances. In order to establish a scaling that can be applied to other impacts not observed by the PPR, we might also determine a scaling between the total fireball radiant energy or the peak 945-rim flux (Fig. 6) and other characteristics of the observed ground-based lightcurves. One of these, for example, would be a scaling between the peak 945-11111 flux and the peak observed flux in the "first precursor", representing the earth-based view of the bolide radiation, or the "second precursor", representing the earth-based view of the fireball radiation (Nicholson 1995a).

There is a wealth of available data. Table 2 lists all the observations made of the Galileo-observed impacts, although not all these data sets have been published yet. Observations of both precursors were made by several observatories at 2.3- μ m, a wavelength that was popular because radiation from Jupiter's disk is minimized by strong CH₄ and H₂ absorption. Among the impact phenomena observed by the PPR at 945 nm, only the first precursors for H and L were observed and calibrated radiometrically, and those were from Calar Alto (Hamilton et al. 1995). Second precursors, characterizing the radiation emitted by the fireball rising over the planetary limb, were observed for the G, H, L, and Q 1

impacts at Calar Alto (Hamilton et al. 1995), Mt. Stromlo (McGregor et al. 1995), and the S. African Astronomical Observatory (Takeuchi 1996).

Is it possible to establish a universal scaling? Figure 7 shows the relationship between the peak 945-nm flux observed by the PPR and the peak 2.3- μm flux measured by the various ground-based observatories. For both the H and L observations, the highly sampled and relatively accurate lightcurves observed at Pic du Midi (Drossart et al. 1995) were normalized to the calibrated flux observed by Hamilton et al. (1995); this was important for the L event, as the Pic du Midi observations included a pronounced second-precursor local maximum at a point where there was a hiatus in the Calar Alto measurements.

The substantially non-linear nature of the relationship shown in Fig. 7 is unexpected, particularly given the mere 20% difference between the peak 945-nm fluxes of the G and L impacts (Fig. 6). While it is the L impact radiance that appears to digress from linearity the most, it is the G impact radiance that is likely to be too low, as the data at 2.3 μm are derived only from the Mt. Stromlo observations (McGregor et al. 1995), which have a coarser time sampling than the other observations. The uncertainties characterizing the absolute radiometric calibration of many of these results are unreported. As we demonstrate below, several observations of the same event at a wavelength of 2.3 μm show differences of the peak flux on the order of 50%. Keeping that in mind, the PPR 945-nm flux of the R impact (recorded but not returned to Earth) is probably on the order of $1.1 \times 10^{-14} \text{ W m}^{-2} \text{ nm}^{-1}$, based on the well-established Kock observation of the second precursor flux (Graham et al. 1995), which is about $8 \times 10^{-13} \text{ W m}^{-2} \text{ nm}^{-1}$. The relationships suggested by Fig. 6 and Fig. 7 together can also provide a means for relating this value to the total radiant energy loss in the bolide/fireball phase for impacts not observed by Galileo. Further data from the SPIREX South Pole astronomical station, which covered the largest number of impact events, might help further to verify this scaling.

Fallback ("Main Event") Phase

A fairly sophisticated physio-chemical model is required to describe the radiation emerging from both continuum and line emission sources during the atmospheric shock re-entry of atmospheric dust and gas during the fallback stage of each event. Such models do not yet exist. Zahnle (1996) estimates the total impacting energy for fragment R as $\sim 4 \times 10^{26}$ ergs. Estimates of the temperature characteristic of the fallback emission have been derived from NIMS data (Carlson et al. 1995) as 300 K (4-5 μm), or ~ 1000 K (2-4 μm); from Palomar 3-13 μm observation as 550-1000 K (Nicholson et al. 1995b); and from the AAT 2.0- to 2.4- μm spectral observations as 400 K near the start of the fallback event and 600-800 K later (Meadows and Crisp 1995). One of the potential problems with these estimates is a confusion between continuum emission from gases and dust with gaseous line emission, which may also be non-LTE in nature (Meadows and Crisp 1995). Another is a failure to emulate wavelength-dependent emissivity of dust accurately, compounded by a failure to account for weak and unmodelled gaseous continuum absorption or emission at such high temperatures.

Our approach here is more heuristic, with a very limited goal of estimating the fallback energy, using some simplifying but reasonable assumptions. First, we assume that the area of emission is constant with time and defined by the area of the dark visual ejecta (e.g. Hammel et al. 1995) or thermal glow pattern (Orton et al. 1995). Second, we assume a blackbody spectral distribution fit to the spectrum observed over a broad wavelength range. Third, we assume that the emission is isotropic, i.e. arising from an optically thick region, qualitatively consistent with the high opacities required by Zahnle and MacLow (1995) to match the R impact lightcurves at wavelengths between 2.3 and 4.5 μm . The resulting emission is then scaled point-by-point in time to the observed lightcurve. This simple modelling accounts for the basic geometric variation in area of the emitting region visible to the earth-based observer at any given time.

We have combined data sets to create a continuous $\sim 2\text{-}\mu\text{m}$ lightcurve for impacts C, H, K, L and R (Figures 8-12 respectively). While of great interest for comparison with Galileo

results, the only accurate lightcurve for the G impact yet available is from Mt. Stromlo (McGregor et al. 1995). Longer-wavelength observations from Keck and the IRTF extend only to 5 μm , and only part of the lightcurve was observed, under difficult weather conditions. Although of no direct interest for comparison with Galileo results, the C impact lightcurves (Fig. 8) are instructive in the sense that they help to characterize the absolute calibration differences between various observatories. The main event observations from the IRTF (Orion et al. 1995; Goguen 1996) and Okayama (Takeuchi et al. 1995) are in excellent agreement, but the Mt. Stromlo observations are some 50-60% brighter. For the H impact (Fig. 9), the recently reduced lightcurve observed at the S. African Astronomical Observatory is very useful in completing the lightcurve observed only partially without saturation at Calar Alto (Hamilton et al. 1995), and the two agree well where they overlap in time. For the K impact (Fig. 10), the Okayama lightcurve (Takeuchi et al. 1995) is ~ 2 - 2.5 times the Mt. Stromlo lightcurve (McGregor et al. 1995). Weather or divergent calibration systems might be responsible. McGregor et al. warn that the observations of the brightest events may have easily saturated their detector, and their lightcurves might best be considered lower limits - a consideration which should probably be applied to their G impact lightcurve. For the L impact (Fig. 11), we have shown an upward scaling with a small offset in time for the K impact lightcurves given in Fig. 10. These help to fill in the gap where the Calar Alto lightcurve (Hamilton et al. 1995) became saturated. For the R impact main event (Fig. 12), the Keck and Mt. Stromlo lightcurves are in excellent agreement, although the precursor observations recorded by Keck are substantially higher. Thus, though systematic problems such as detector saturation may have created differences as high as factors of 2 - 2.5 in the observations of the brightest impacts, the worst disagreement we note is no more than 60% for the C impact main event. Most of the observations we considered above are consistent with one another at the 10- 20% level.

Estimates of the temperature of the fallback phase are shown in Figures 13 - 16. For most of the observations, this is a crude two-wavelength color temperature. However for the widely observed R impact (Fig. 13), observations span 6 wavelengths between 2.3 and 12.5 μm . Blackbody temperatures between 900 K in the earliest phases and 700 K in the later phases of the R main event are characteristic of the gross spectral shape. The 700-Kelvin blackbody curve, in fact, fits extremely well at fitting the spectrum of the fallback radiation at its peak some 10 min. after impact. At later times, the bright 10.3- μm spectral peak observed at the IRTF (Friedson et al. 1995) likely arises from silicate emission in the fallback material, as seen in the Palomar spectrum (Nicholson et al. 1995b). The impact regions are prominent at this wavelength for many days afterward (Orton et al. 1995). The temperatures for H (Fig. 14), L (Fig. 15) and Q1 (Fig. 16) all use the 11.9- μm observations taken at the Nordic Optical Telescope (Lagage et al. 1995) to determine the color temperature. A reference to Fig. 13 shows that those measurements may miss important emission from the 10- μm region, although the absolute values appear to be higher. These derived temperatures fall within a range roughly bounded by ~ 400 -900 K. The center of this range and its extremes can be used to define broad limits to a spectral distribution that is constant in time. Although it is a simplification of time variable conditions, the range of temperatures in the models is sufficient to define the variation of spectral distribution for most of the main event.

The integration of the total radiative output of the fallback phase can be computed, assuming a spectral distribution derived from a blackbody whose temperature is constant in time, from any single observation set, using

$$E = \pi D^2 \rho \int_{t_0}^{\infty} \frac{\Omega_0}{\Omega(t)} F_{\lambda}^{obs}(\lambda_0, t) dt \quad (2)$$

for the optically thick case, or

$$E = 2 \pi \Delta^2 \rho \int_{t_0}^{\infty} F_{\lambda}^{obs}(\lambda_0, t) dt \quad (3)$$

for the optically thin case, where D = distance to the observer; A = diameter of the emitting area; Ω_0 = solid angle subtended by the emitting area on a plane normal to the line of sight; $\Omega(t)$ = solid angle projected by the emitting area to the observer; $F_{\lambda}^{\text{obs}}(\lambda_0, t)$ = observed flux; and, assuming that F_{λ} is proportional to $B_{\lambda}(T_{\text{eff}})$,

$$P = \frac{\int B_{\lambda}(T_{\text{eff}}) d\lambda}{B_{\lambda}(A_o)}.$$

The value of p is easily determined and is fixed for a given temperature and wavelength (Table 3). The self-consistency of the radiative output for the same impact from a variety of wavelengths using this technique can be used to indicate the extent to which the temperature assumptions are valid, although it is only an alternative means for illustrating the spectral distributions shown in Figs. 13- 16.

The presence of a spectral feature attributable to silicate particles in the spectrum of Nicholson et al (1995b) and their solution for the optical thickness of the emitting layer, $\tau = 0.02$, favor the optically thin approximation. Note that Eq. (3) is equivalent to Eq. (3) of Nicholson et al (1995b) without the wavelength dependence of emissivity.

To first order, we would expect the estimate of the total radiative energy output to be independent of the size or geographic distribution of the emitting area. Even for the optically thick approximation (Eq. 2), it is only the ratio of the emitting area to its projection toward the earth-based observer that matters; the product of the radiative power and the emissivity are subsumed together and constrained by the observation itself. However, in the first few minutes of the observation, it is clear from Figs. 9- 12 that the emitting area is not even past the planetary limb and the effective emitting area must be well beyond the single point of impact. This implies that the estimate must include radiation not observable from the earth if the emitting area is optically thick. On the other hand, both the earth-based fallback lightcurves for G and R and those of the NIMS instrument show similar times for the onset of the "main event", demonstrating that there were probably no "main event" phenomena unobserved from the earth. It is also probable in an optically thin case that when the impact site is still nominally behind the limb, its altitude is sufficiently high that it can be detected from the earth, gaseous attenuation by H_2 absorption and Rayleigh scattering being negligible at these wavelengths.

We can place some limits on the emitting region. It is clear from the earliest impacts, which were farthest from the limb, such as C (Fig. 8), that the rise of the main event lightcurve occurred while the impact point was some $6-7^{\circ}$ in longitude from the planetary limb. Observations at various wavelengths made at the IRTF show that the emission is generally coincident with the regions that are visually dark with impact ejecta (e.g. Hammel et al. 1995), at least late in the lightcurve. For the purposes of this review, we make two limiting assumptions: (1) the fallback radiation is uniformly distributed around the area within 7° of the impact site, (2) the radiance is uniformly distributed around an area within 13° of the impact site, this value corresponding to a rough mean over impacts for the outermost limit of the dark ejecta "fan" from the impact site. We note that it is possible that the emission has a non-uniform spatial distribution. The areas closest to the impact point appeared brighter than the ejecta regions in the IRTF data. However, this distribution has not yet been measured, and for now we retain our more simple assumption of uniform brightness.

Table 4 shows the results of this approach. It is clear that the 2.2 and 2.3- μm observations are most sensitive to the various assumptions about the blackbody temperature controlling the spectral distribution. The difference between the sizes of the emitting disk appears to make at most a 30% difference in the results. However, we caution that the

emission is not radially symmetric about the impact point. The broadly observed R impact shows the greatest internal consistency if one assumes a relatively high value for the equivalent blackbody temperature, about 800 - 900 K, with values of 1×10^{25} erg. However, this result is relatively low; for example, it is comparable to the energy derived from the Q 1 impact. This is largely the result of the lower longer-wavelength flux for R from the IRTF (Friedson et al. 1995), relative to those of the Nordic Optical Telescope (Lagage et al. 1995) for the other impacts. The appropriate choices for the other two-color "spectra" are less obvious, and our adopted values for the single-color observations are simply taken from the 650-K "mean" temperature. Such a level of approximation does not warrant detailed intercomparisons between the total impact energies of the various impacts.

Despite the fact that these numbers are probably uncertain by up to an order of magnitude, some conclusions can be reached. First, the numbers are consistently larger than those for the bolide/fireball stage. This is both a result of the length of this phase in time and the much larger area covered by the emission (Zahnle and MacLow 1995). For the L impact, Bézard et al. (1996) have estimated that the total energy deposited by the impact into the thermalization of the stratosphere is about 3×10^{26} ergs, implying, to the uncertainties of this crude numerical review of the data, a rough equipartition of the energy between the fallback phase radiation and atmospheric heating.

The radiant energy estimates may be equivalence to the kinetic energy of a fractional part of the initial fragment. This forms a strong lower limit to the mass of the fragment. Assuming an initial entry speed of 60 km/sec, the largest impact fragment (L) would require 2×10^{13} gm to supply the energy radiated in the fireball and fall back phases. The smallest of the set described here (R) would require a mass at least 7×10^{11} gm. At a density of 0.5 gm/cm^3 (Asphaug and Benz, 1994; Solem, 1994), these masses imply diameters of 210 and 70 m, respectively, but we emphasize that mass is the more strongly constrained parameter.

It is interesting to compare the relative contribution of the fireball radiation, well observed by Galileo, and the larger fallback phase infrared radiation. For G, we calculate that the fireball radiant energy was 4% of the total. On this basis, it seems unlikely that the earthbased observers missed a large part of the radiated energy.

Future work.

There is clearly more work that can be done to determine a better spectral distribution, the best being simple models to fit data from diverse spectral regions, such as those from the Anglo-Australian Telescope (Meadows et al. 1995), Palomar (Nicholson et al. 1995), and the Kuiper Airborne Observatory (Sprague et al. 1996) broad spectra of the various impacts. However, there are also additional data sets, including the South Polar SPIREX data at 2.22 and $2.36 \mu\text{m}$ (Severson 1996), and European Southern Observatory TIMMI data at $10 \mu\text{m}$ (Livengood et al. 1995), that have yet to be published in a final calibrated form. A quantitative check can be made on the accuracy of models for the earliest radiation from the fireball in the case of the G and R impacts by comparing with NIMS observations.

We thank several investigators and their teams for making data available to us in numerical form: J. Graham and I. de Pater, P. Lagage, P. McGregor, P. Nicholson, and S. Takeuchi - particularly for his S. African Astronomical Observatory lightcurves in advance of their publication. We also thank K. L. Jessup for information on the distribution of impact ejecta, and R. Carlson for suggesting the importance of cloud reflection. This review was funded by the Galileo Project Office and This research was carried out by the Jet Propulsion Laboratory, California Institute of Technology, under a contract with the NASA Office of Space Science, Planetary Astronomy Discipline through the Shoemaker-Levy 9 Data Analysis program.

References

- Ahrens, T. J., et al, Impact of comet Shoemaker-Levy 9 on Jupiter, *Geophys. Rev. Lett.*, 21 1087 (1994).
- Asphaug, E. and W. Benz, Density of comet Shoemaker Levy 9 deduced by modeling breakup of the parent 'rubble pile', *Nature*, 370 120-124(1994).
- Bézar, B., C. A. Griffith, D. Kelly, J. Lacy, T. Greathouse, and G. Orton. Thermal infrared imaging spectroscopy of Shoemaker-Levy 9 impact sites: Temperature and HCN retrievals. *Icarus* 125, 94-120 (1997).
- Borovicka, J. and P. Spurný, Radiation study of two very bright terrestrial bolides and an application to the comet SL9 collision with Jupiter, *Icarus* 121484 (1996).
- Boslough, M. B., D.A. Crawford, T.G. Trucano, and A.C. Robinson, Numerical modeling of Shoemaker-Levy 9 impacts as a framework for interpreting observations, *Geophys. Rev. Lett.*, 221821 (1995).
- Carlson, R.W. *et al*, Galileo infrared observations of the comet Shoemaker-Levy 9 G impact fireball: a preliminary report, *Geophys. Rev. Lett.*, 22 1557 (1995a).
- Carlson, R. W., private communication (1995b).
- Chapman et al, Preliminary results of Galileo direct imaging of SL 9 impacts, *Geophys. Rev. Lett.*, 221561 (1995).
- Chevalier, R.A. and C.L. Sarazin, Explosions of infalling comets in Jupiter's atmosphere, *Astrophys. J.* 429863 (1994).
- Drossart, P., T. Encrenaz, L. Lecacheux, F. Colas, and P. O. Lagage. The time sequence of SL9/impacts H and L from infrared observations. *Geophys. Res. Lett.* 22, 1769(1995).
- Friedson, A. J., W. F. Hoffmann, J. D. Goguen, K. K. Deutsch, G. S. Orton, J. L. J. Iora, A. Dayal, J. N. Spitale, W. K. Wells, and G. G. Fazio. Thermal infrared lightcurves of the impact of Comet Shoemaker-Levy 9 fragment R. *Geophys. Res. Lett.* 22, 1569 (1995).
- Goguen, J. Unpublished communication (1996).
- Graham, J. R., I. de Pater, J. G. Jernigan, M. C. Liu and M. E. Brown. The collision of fragment R of Comet P/Shoemaker-Levy 9 with Jupiter observed by the W. M. Keck Telescope. *Science* 367, 1320-1323 (1995).
- Hamilton, D. P., T. M. Herbst, H. Boehnhardt, and J. L. Ortiz-Moreno. 1995. Calm Alto observations of Shoemaker-Levy 9 - Characteristics of the H-impact and L-impact. *Geophys. Res. Lett.* 22,2417-2420. (1995).
- Hammel, H. B., R. F. Beebe, A. O. Ingersoll, G. S. Orton, J. R. Mills, A. A. Simon, P. Chodas, J. T. Clarke, B. DeJong, T. E. Dowling, J. Harrington, L. F. Huber, E. Karkoschka, C. M. Santori, A. Toigo, D. Yeomans, and R. A. West. Hubble Space Telescope Imaging of Jupiter: Atmospheric phenomena created by the impact of Comet Shoemaker-Levy 9. *Science*. 267, 1288-1296. (1995).
- Herd, C. W. *et al*, Direct observations of the comet Shoemaker-Levy 9 fragment G impact by Galileo UVS, *Geophys. Rev. Lett.*, 221565 (1995).
- Karkoschka, E., Spectrophotometry of the Jovian planets and Titan at 300 to 1000 nm wavelength: the methane spectrum, *Icarus* 111174 (1994).

Lagage, P. O., Ph. Galdemard, E. Pantin, R. Jouan, P. Masse, M. Sauvage, G. Oloffson, M. Hultgren, L. Nordh, J. A. Belmonte, C. Regulo, J. M. Rodrigues Espinosa, L. Vidal, B. Mosser, A. Ulla and D. Gautier. SL-9 fragments A, E, H, L, Q1 on to Jupiter: Mid-infrared light curves. *Geophys. Res. Lett.* 22, 1773-1776. (1995).

Livengood, T. A., H. U. Käufl, G. Wiedemann, B. Mosser, M. Sauvage, T. Kostiuk, G. L. Bjoraker, and P. N. Romani. 1995. Multi-wavelength thermal-infrared imaging of SL-9 impact phenomena. In *European SL-9/Jupiter Workshop*. ESO Special Publication, pp. 137-146.

Martin, T. Z., G.S. Orton, L.D. Travis, L.K. Tamppari, and I. Claypool, Observation of Shoemaker-Levy impacts by the Galileo Photopolarimeter Radiometer, *Science*, 268 1875 (1995).

McGregor, P. J., P. D. Nicholson, and M. G. Allen. CASPIR observations of the collision of comet Shoemaker-Levy-9 with Jupiter. *Icarus* 121, 361-388 (1996).

Meadows, V. and D. Crisp. Impact plume composition from near-infrared spectroscopy. In *Proceedings of the European SL-9/Jupiter Workshop* (R. West and J. Bohnhardt, Eds.) p. 239. EOS, Garching (1995).

Nicholson, P. D., P. J. Gierasch, T. L. Hayward, C. A. McGhee, J. E. Moersch, S. W. Squires, J. VanCleve, K. Mathews, G. Heugebauer, D. Shupe, A. Weinberger, J. W. Miles and B. J. Conrath. Palomar observations of the R impact of comet Shoemaker-Levy-9.1. *Lightcurves. Geophys. Res. Lett.* 22, 1613-1617 (1995a).

Nicholson, P. D., P. J. Gierasch, T. L. Hayward, C. A. McGhee, J. E. Moersch, S. W. Squires, J. VanCleve, K. Mathews, G. Heugebauer, D. Shupe, A. Weinberger, J. W. Miles and B. J. Conrath. Palomar observations of the R impact of comet Shoemaker-Levy-9.11. *Spectra. Geophys. Res. Lett.* 22, 1617-1620 (1995 b).

Orton, G. S., M. A'Hearn, K. Baines, D. Deming, T. Dowling, J. Goguen, C. Griffith, H. Hammel, W. Hoffmann, D. Hunten, D. Jewitt, T. Kostiuk, S. Miller, K. Nell, K. Zahnle, N. Achilleos, A. Dayal, L. Deutsch, F. Espenak, T. Esterle, J. Friedson, K. Fast, J. Harrington, J. Hora, R. Joseph, D. Kelly, R. Knacke, J. Lacy, C. Lisse, J. Rayner, A. Sprague, M. Shure, K. Wells, P. Yanamandra-Fisher, D. Zipoy, G. Bjoraker, D. Buhl, W. Golisch, D. Griep, C. Kaminski, C. Arden, A. Chaikin, J. Goldstein, D. Gilmore, G. Fazio, T. Kanamori, H. Lam, T. Livengood, M.-M. MacLow, M. Marley, T. Momary, D. Robertson, P. Romani, J. Spitale, M. Sykes, J. Tennyson, D. Wellnitz, and S.-W. Ying. The NASA Infrared Telescope Facility investigation of Comet Shoemaker-Levy 9 and its collision with Jupiter. *Science*, 267, 1277 (1995).

Solem, J. C., Density and size of Comet Shoemaker-Levy 9 deduced from a trial breakup model, *Nature*, 370 349-351 (1994).

Sprague, A. P., G. L. Bjoraker, D. M. Hunten, F. C. Witteborn, and R. W. H. Kozlowski. Water brought into Jupiter's atmosphere by fragment-R and fragment-W of Comet Shoemaker-Levy 9. *Icarus* 121, 30-37 (1996).

Severson, S. A., M. Hereld, H. Nguyen, B. J. Rascher. SPIREX observations of the collision of comet Shoemaker-Levy 9 and Jupiter. *Bull. AAS*, 27, 1115 (1995).

Takeuchi, S., H. Hasegawa, J. Watanabe, T. Yamashita, M. Abe, Y. Hirota, E. Nishihara, S. Okumura, and A. Mori. Near-IR imaging observations of the cometary impact into Jupiter: Time variation of radiation from impacts of fragments C, D and K. *Geophys. Res. Lett.* 22, 1581 (1995).

Takeuchi, S. Personal communication. (1996).

Zahnle, K and M. M. Maclow. A simple model for the light-curve generated by a Shoemaker-Levy-9 impact. J. Geophys. Res. 100, 16885-16894 (1995).

Livengood, T. A., H. U. K^u, G. Wiedemann, B. Mosser, M. Sauvage, T. Kostiuk, G. L. Bjoraker, and P. N. Romani. 1995. Multi-wavelength thermal-infrared imaging of SL-9 impact phenomena. In European SL-9/Jupiter Workshop. ESO Special Publication.

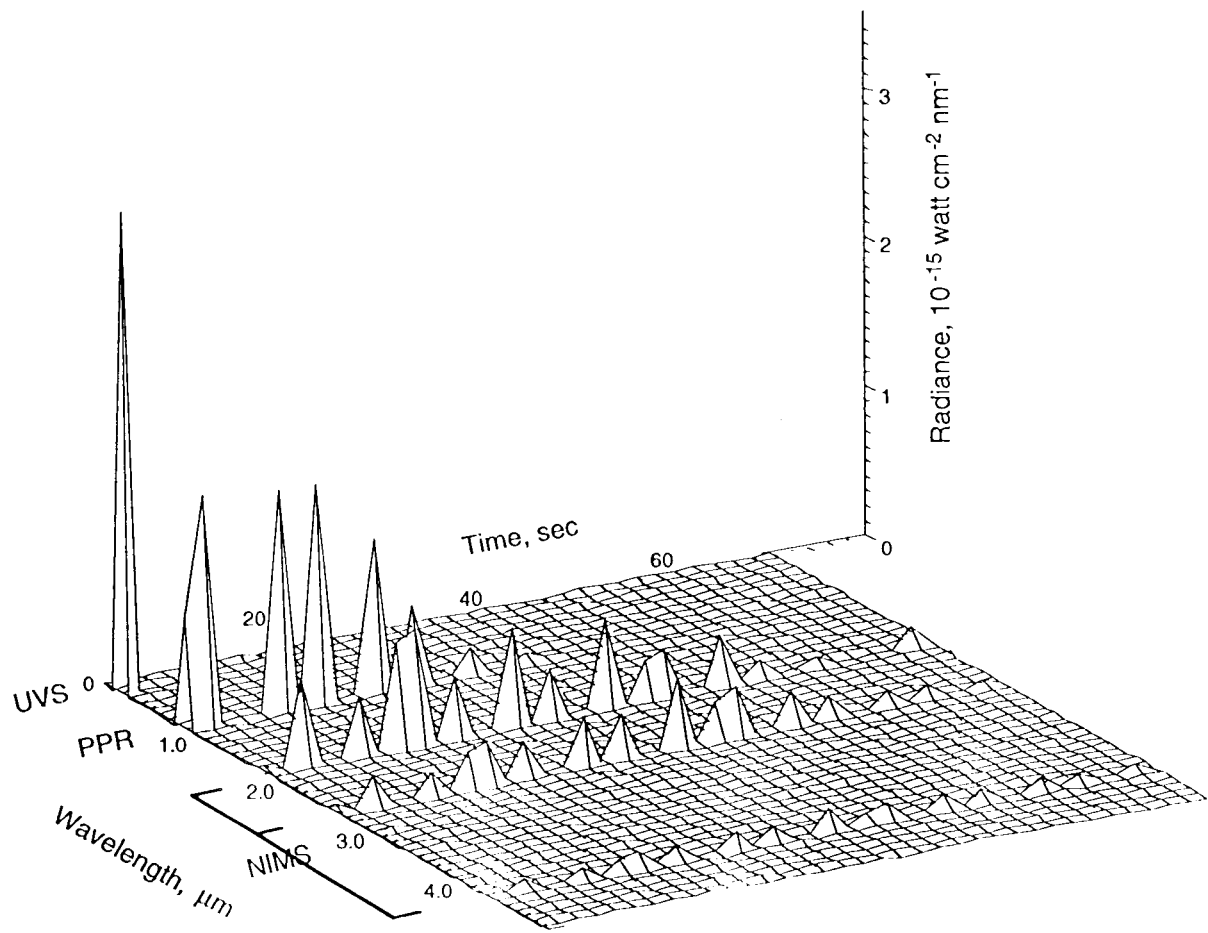


Fig. 1. Radiance data from the Galileo UVS, PPR, anti NIMS experiments for the fragment G impact event.

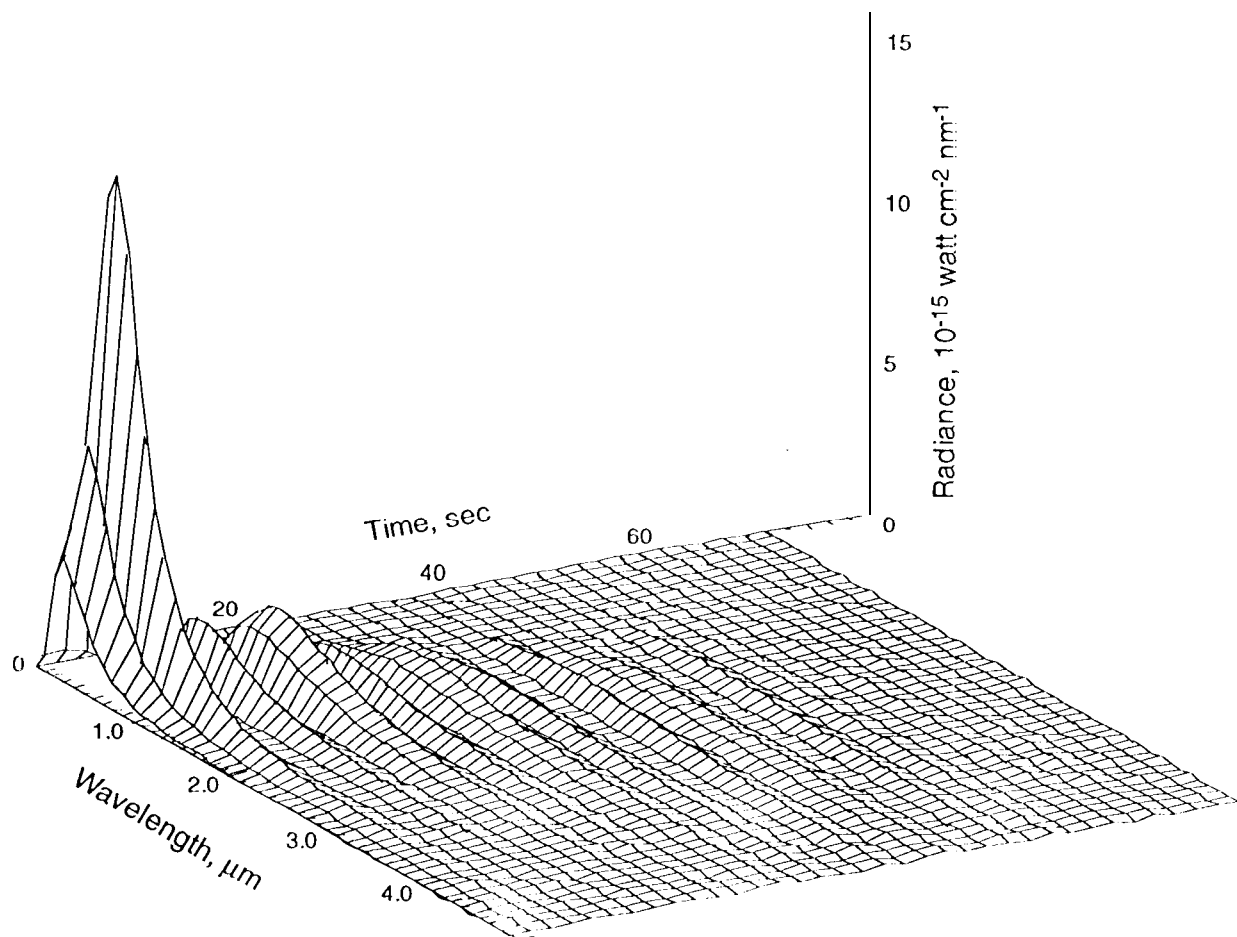


Fig. 2. Model of the spectral energy distribution for the G impact, obtained by fitting the data shown in Fig. 1. Note different vertical scale.

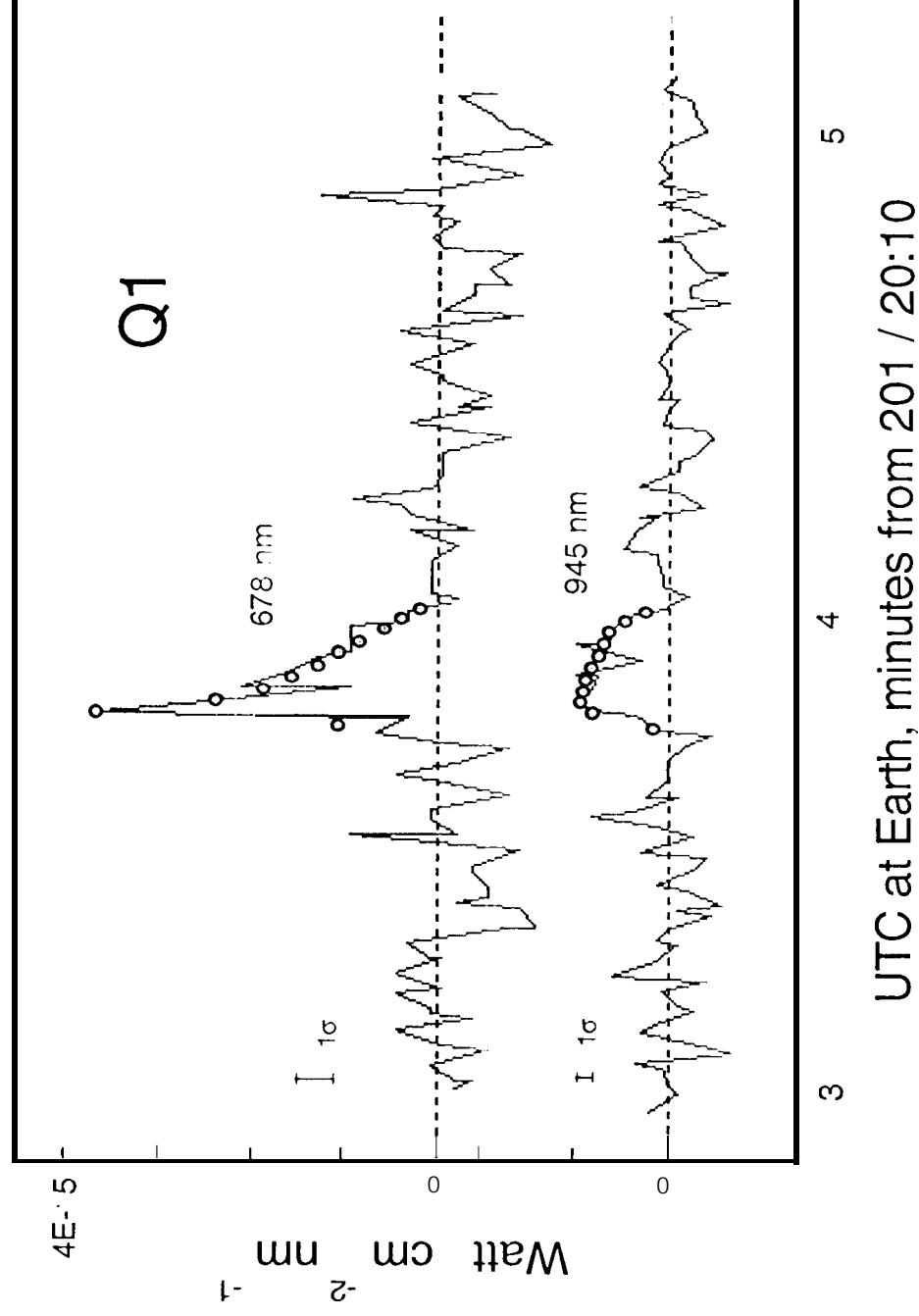


Fig. 3. Smoothing of the 678 and 945 nm PPR data for the fragment Q1 impact. Each curve is the average of the two orthogonal polarization channels of the PPR. Jupiter was viewed alternately in each wavelength; the polarization channels were simultaneously sampled. The sample interval was 1.26 s for a given filter.

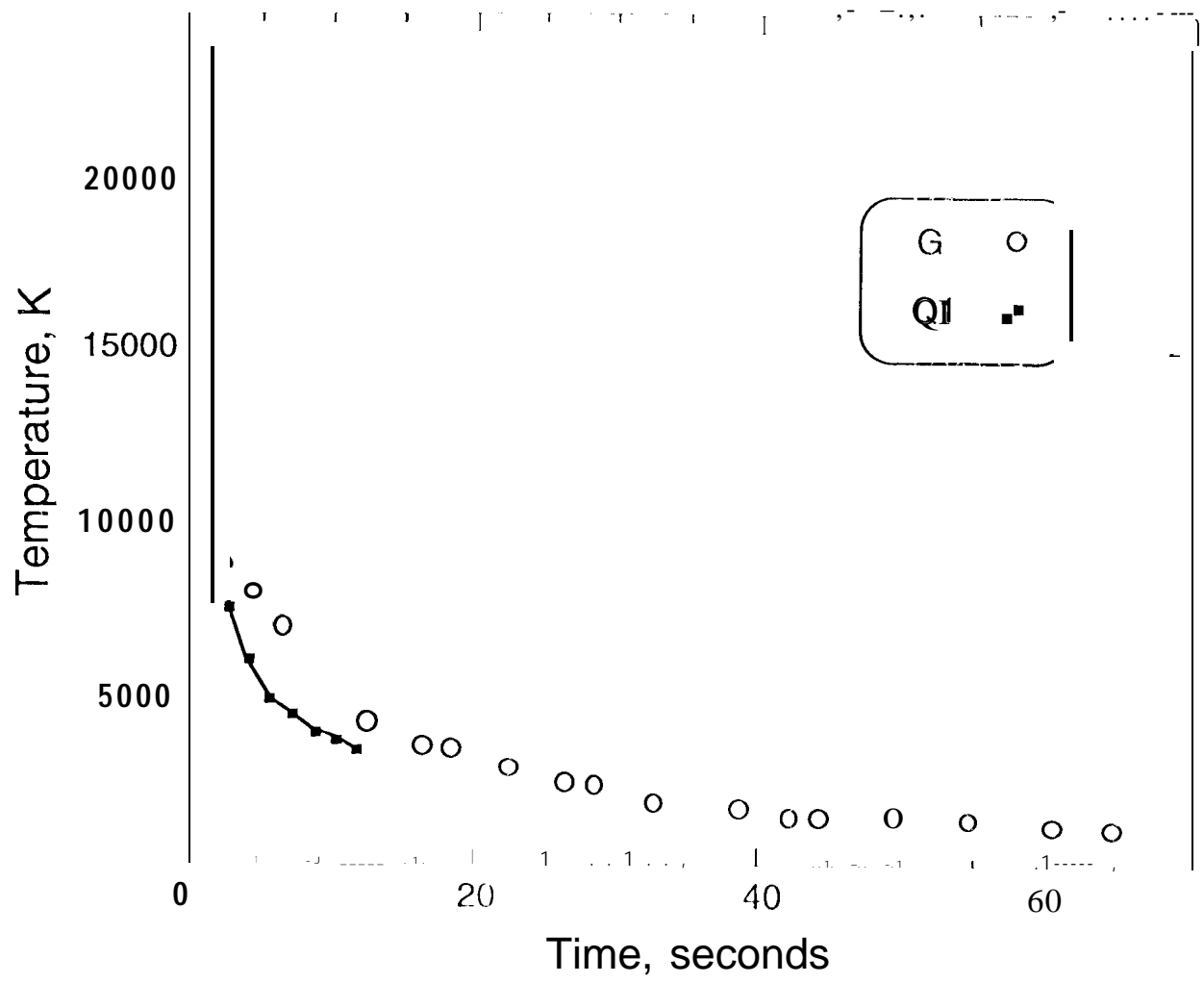


Fig. 4. Temperatures of the G and Q1 fireball Is,

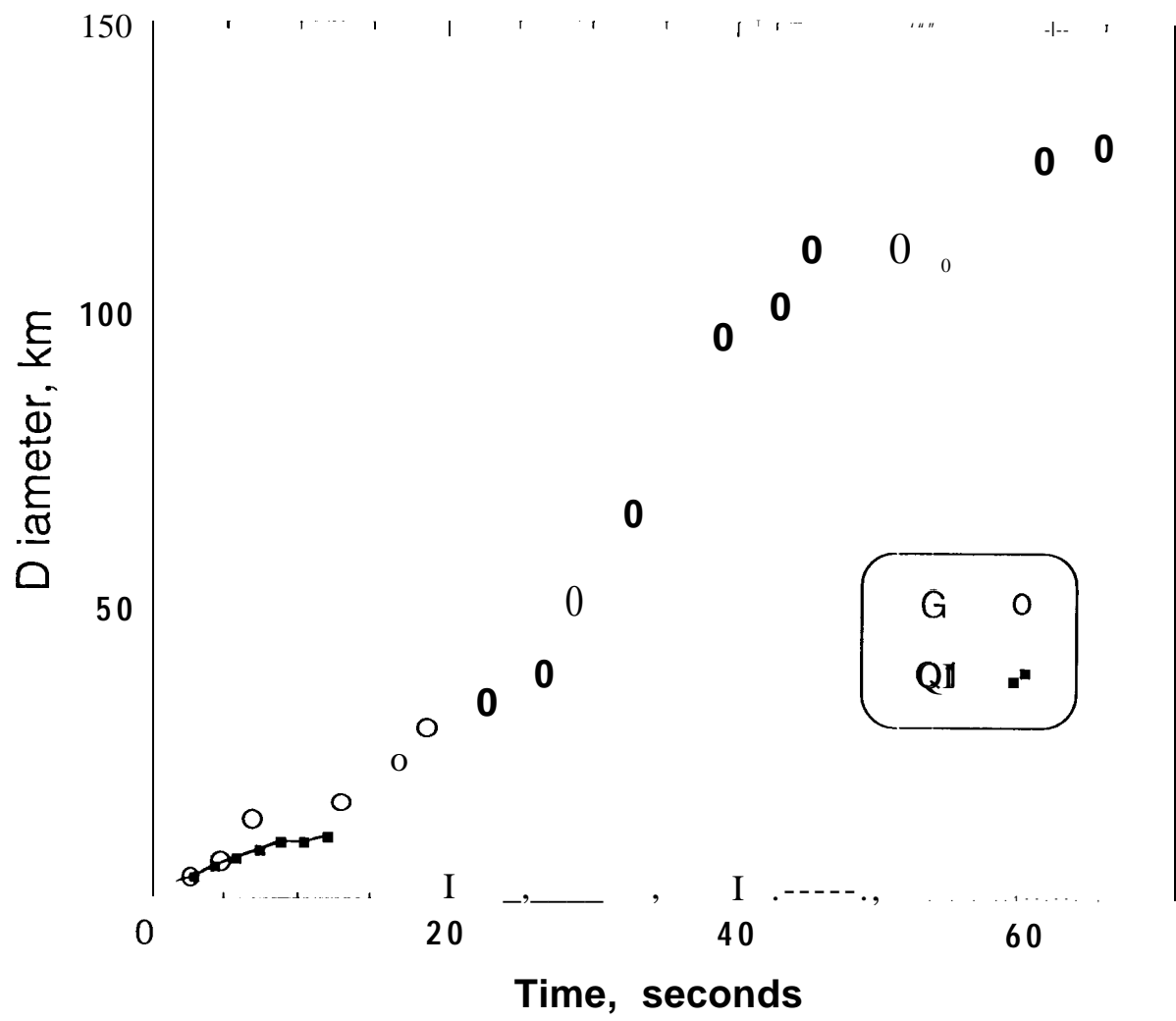


Fig. 5. Diameters of the G and Q1 fireballs.

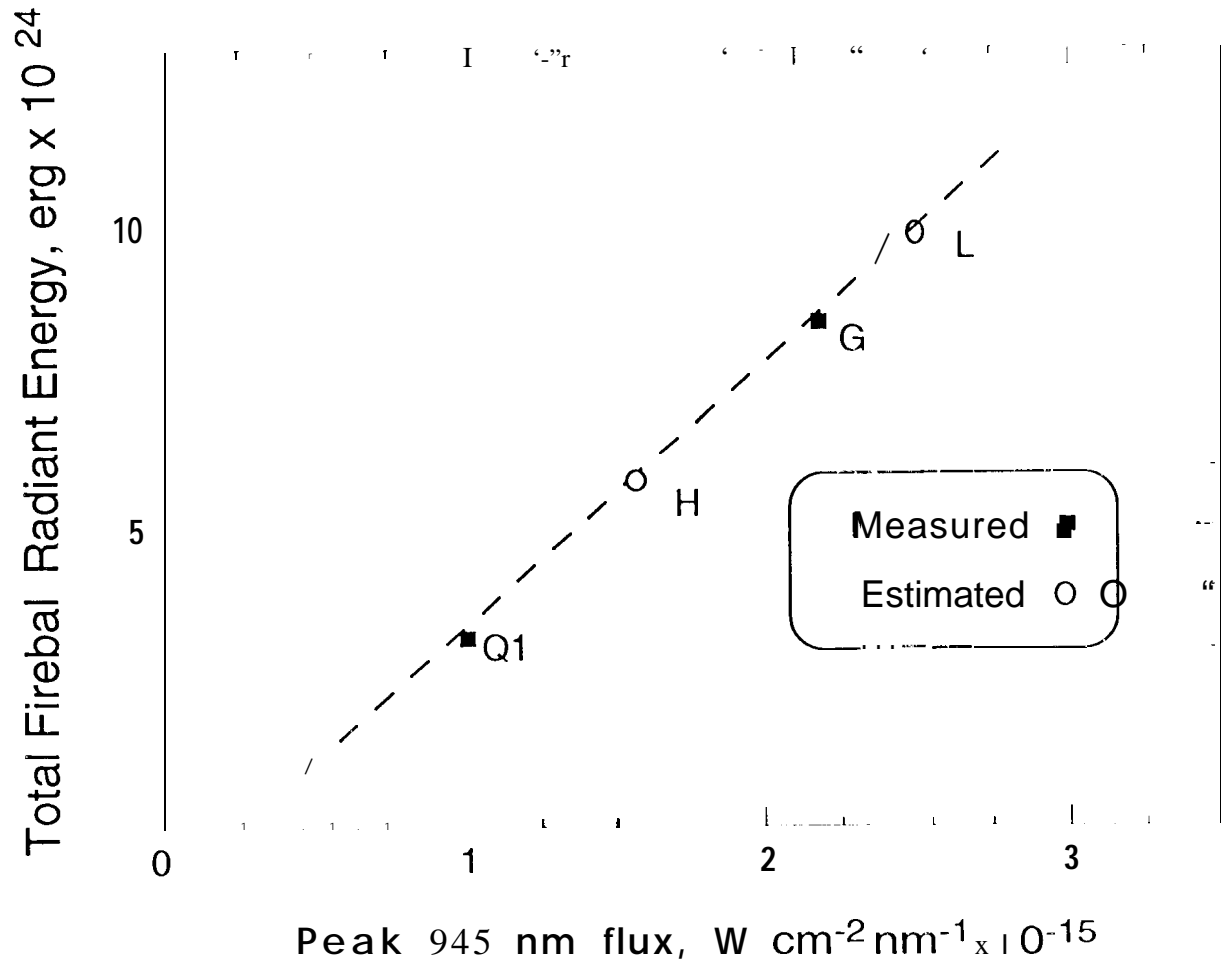


Fig. 6. Dependence of total radiant energy on peak 945 nm flux. G and Q 1 energies are derived from the observed spectrum evolution, and H and L energies are inferred from their peak flux measurements.

Figure 7. Plot of the peak “second precursor” flux measured from various ground-based observatories near $2.3\ \mu\text{m}$ vs tile bolide/fireball flux measured at $945\ \text{nm}$ by the Galileo Photopolarimeter/Radiometer. A curve going through most of the data is also shown. The small inconsistency of this curve with the measured Q 1 points may be a result of the larger uncertainties associated with the relatively faint Q 1 event.

Figure 8. The lightcurves for the C impact observed at $2.3\ \mu\text{m}$ at Mt. Stromlo / Siding Spring Observatory (McGregor et al. 1995; filled circles), Okayama Astrophysical Observatory (Takeuchi et al. 1995; open circles), and the NASA Infrared Telescope Facility (Orton et al. 1995; Goguen, 1996; filled diamonds). The time corresponding to the impact point crossing Jupiter’s limb onto the observable disk is noted by the vertical dashed line in this figure and in Figs. 9- 12. Note the good agreement between the Okayama and IRTF observations for the main event; the Mt. Stromlo observations are some 55% higher.

Figure 9. The lightcurves for the H impact observed at $2.3\ \mu\text{m}$ at Calar Alto Observatory (Hamilton et al. 1995; filled circles), Pic du Midi Observatory (Drossart et al. 1995; filled diamonds), and the South African Astronomical Observatory (Takeuchi 1996; open circles). The Pic du Midi data lack absolute radiometric calibration and have been fitted to the other data sets using a constant best fit scaling factor. Note the excellent agreement between the absolute radiometric calibration of the Calar Alto and South African data.

Figure 10. The lightcurves for the K impact observed at $2.3\ \mu\text{m}$ at Mt. Stromlo / Siding Spring Observatory (McGregor et al. 1995; filled circles) and at Okayama Astrophysical Observatory (Takeuchi et al. 1995; open circles). The Okayama observations appear to be some 2 -2.5 times higher than those of the main event observed at Mt. Stromlo.

Figure 11. The lightcurves for the L impact observed at $2.3\ \mu\text{m}$ at Calar Alto Observatory (Hamilton et al. 1995; open circles) and Pic du Midi Observatory (Drossart et al. 1995; filled diamonds). Just as for the H impact, the Pic du Midi data lack absolute radiometric calibration and have been fitted to the Calar Alto data set using a constant best fit scaling factor. The Okayama and Mt. Stromlo K lightcurves presented in Fig. 10 are also given here after being scaled upward by a factor of 2.5. The agreement between the morphology of the more fully observed K lightcurves and the incomplete observations of the L lightcurve is sufficient to use the scaled K observations as a substitute for a directly observed lightcurve for the purpose of integrating the total lightcurve radiance.

Figure 12. The lightcurves for the R impact observed at $2.3\ \mu\text{m}$ at Mt. Stromlo / Siding Spring Observatory (McGregor et al. 1995; filled diamonds) and the W. M. Keck Observatory (Graham et al. 1995; filled circles). Note the good agreement between these lightcurves for the peak of the main event, although there are large differences in the observed precursor flux.

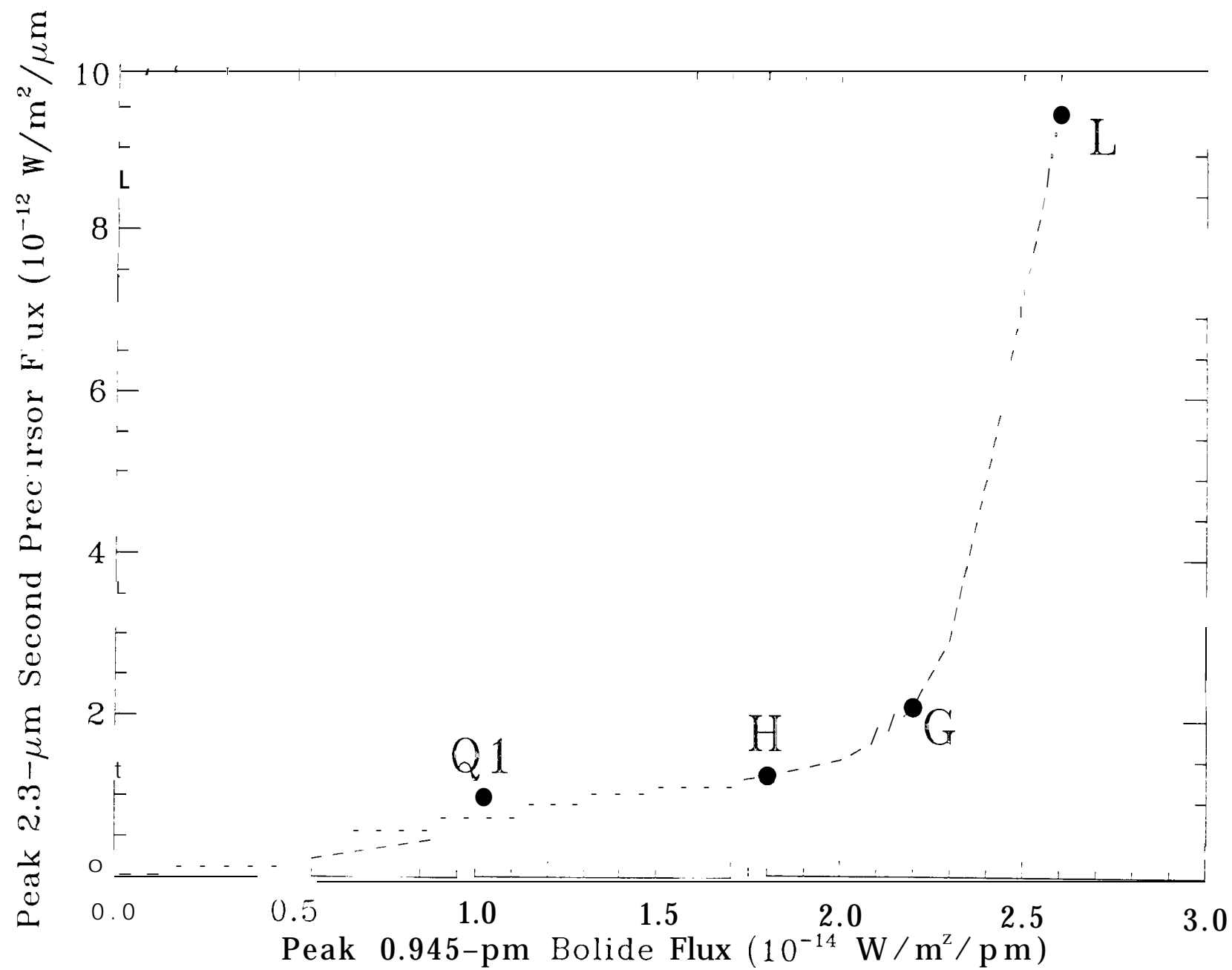
Figure 13. Radiometric observations of the R impact at different moments in the “main event” lightcurve for the range of observed wavelengths. This plot incorporates data from Mt. Stromlo (McGregor et al. 1995), Keck (Graham et al. 1995), Palomar (Nicholson et al. 1995), and the NASA IRTF (Friedson et al. 1995). An approximate best-fit color temperature is also shown with the crude spectrum shown at each time step in this figure and in Figs. 14- 19.

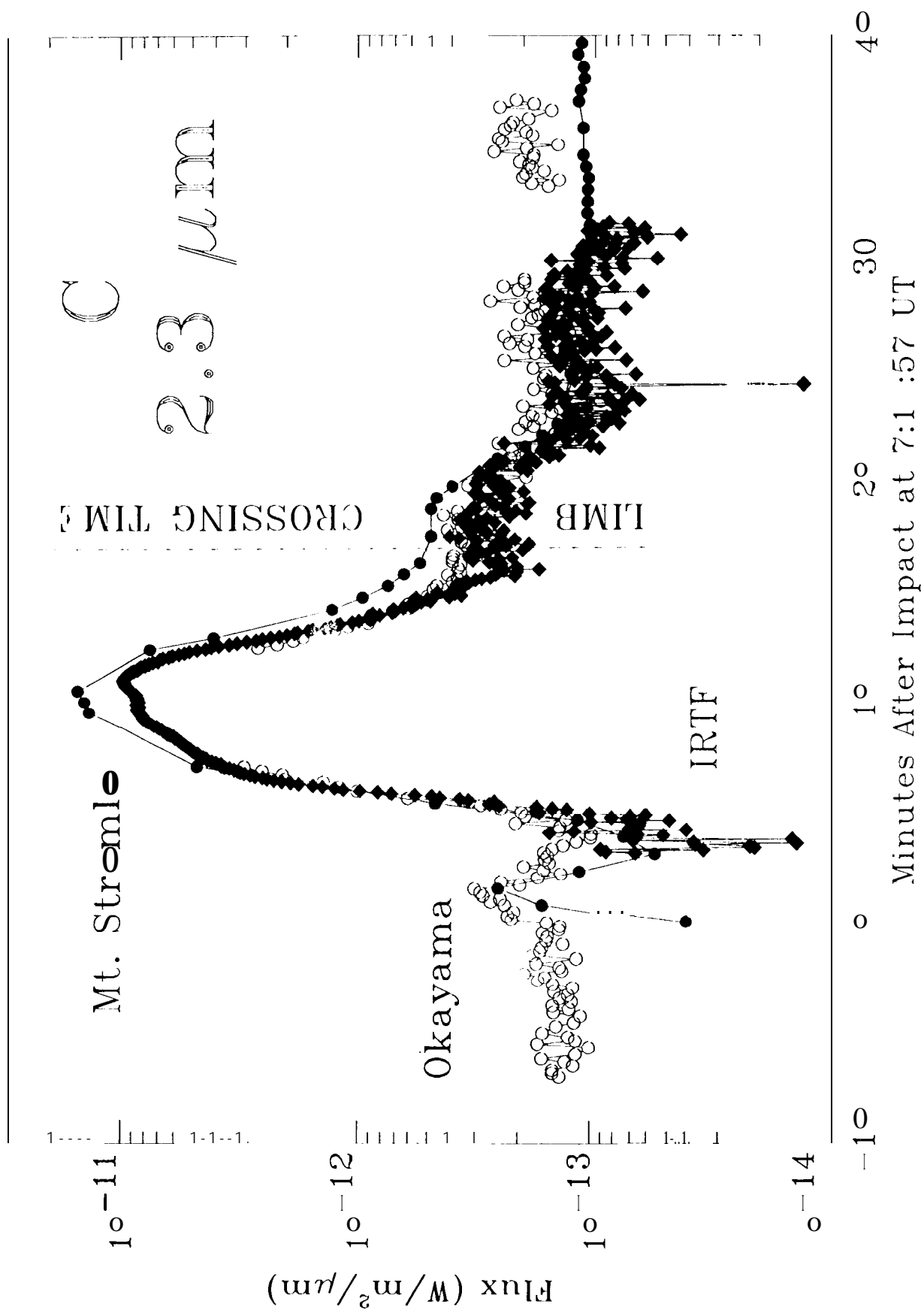
Figure 14. Radiometric observations of the H impact at different moments in the lightcurve for the range of observed wavelengths. This plot incorporates data from Calar Alto (Hamilton et al. 1995), Pic du Midi (Drossart et al. 1995, scaled as shown in Fig. 9), S. African Astronomical Observatory (Takeuchi 1996), and the Nordic Optical Telescope (Lagage et al. 1995).

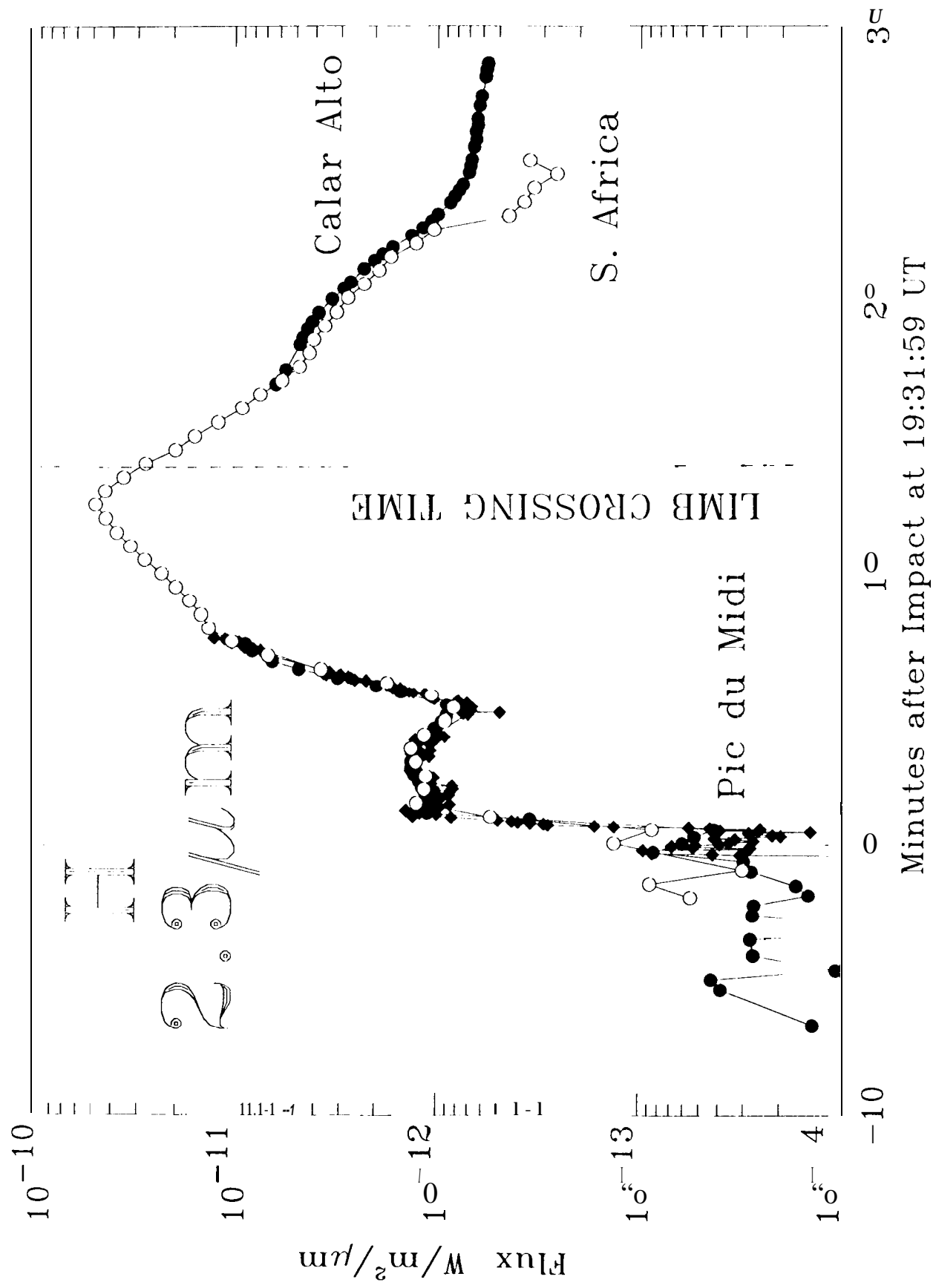
Figure 15. Radiometric observations of the L impact at different moments in the lightcurve for the range of observed wavelengths. This plot incorporates data from Calar Alto (Hamilton et al. 1995), Pic du Midi (Drossart et al. 1995, scaled as shown in Fig. 9), the Nordic Optical Telescope (Lagage et al. 1995), and the average of K impact observations at Okayama

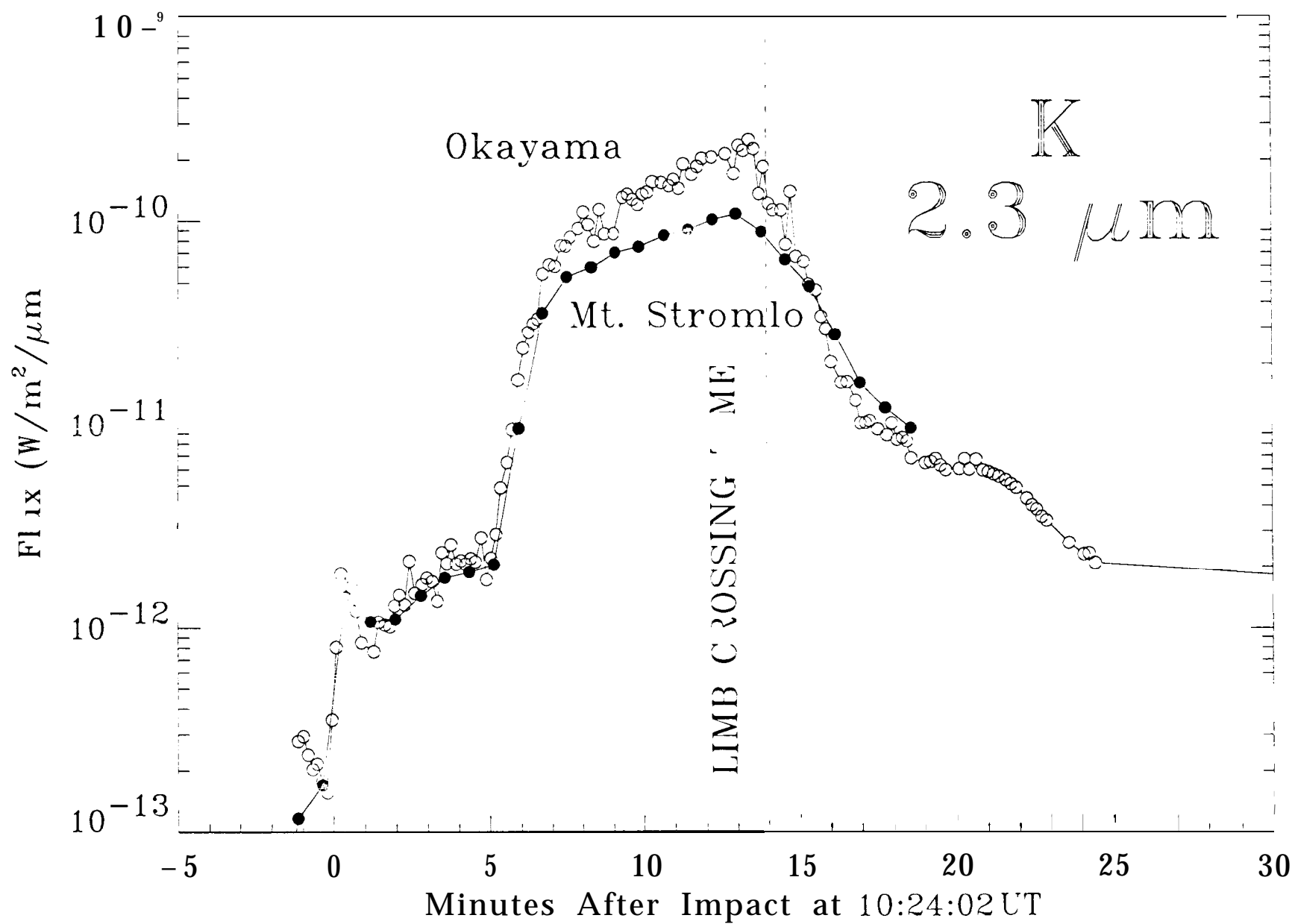
Astrophysical Observatory (Takeuchi et al. 1995) and Mt. Stromlo / Siding Spring Observatory (McGregor et al. 1996), scaled as shown in Fig. 10.

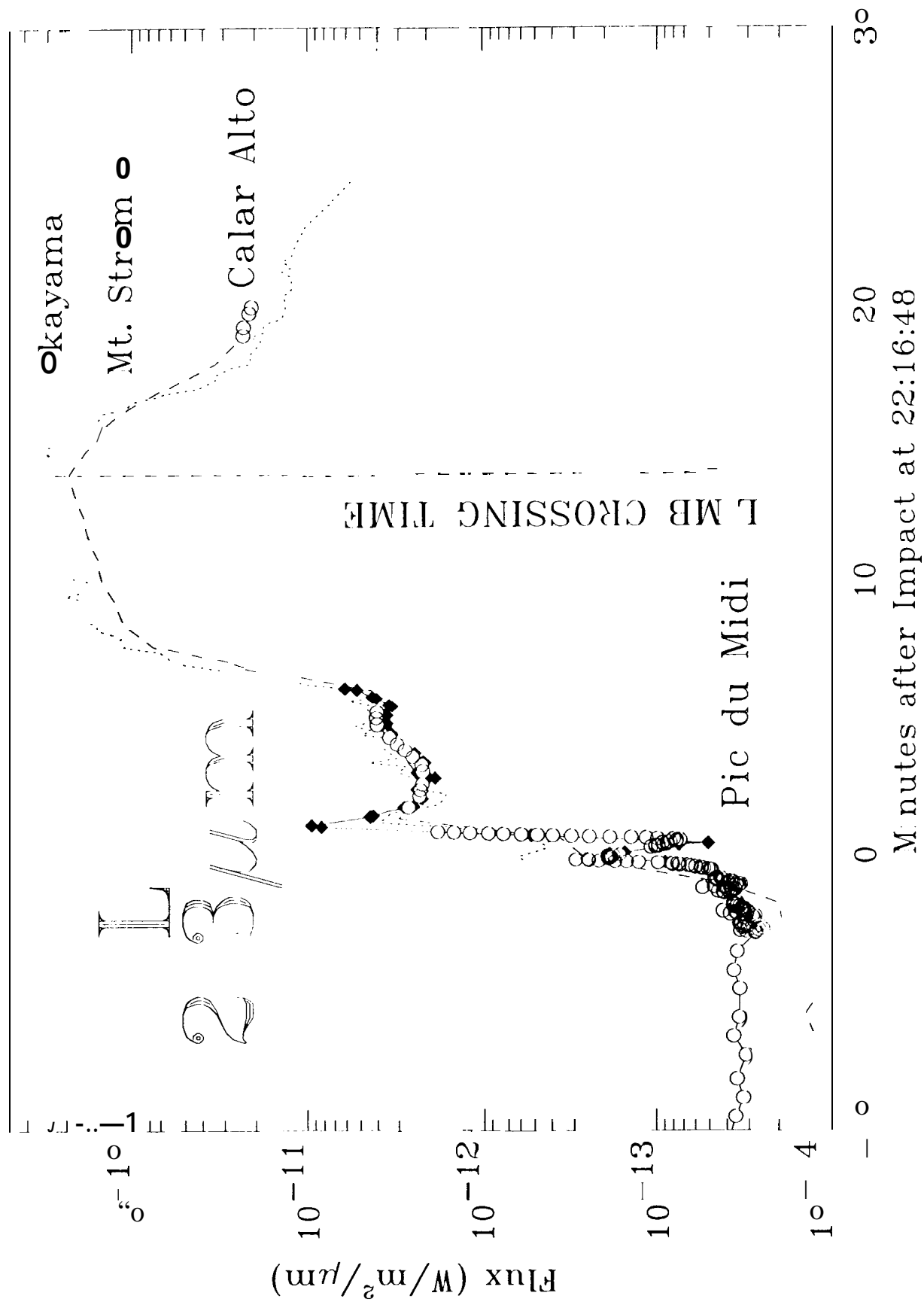
Figure 16. Radiometric observations of the Q 1 impact at different moments in the lightcurve for the range of observed wavelengths. This plot incorporates data from the S. African Astronomical Observatory (Takeuchi 1996) and the Nordic Optical Telescope (Lagage et al. 1995).

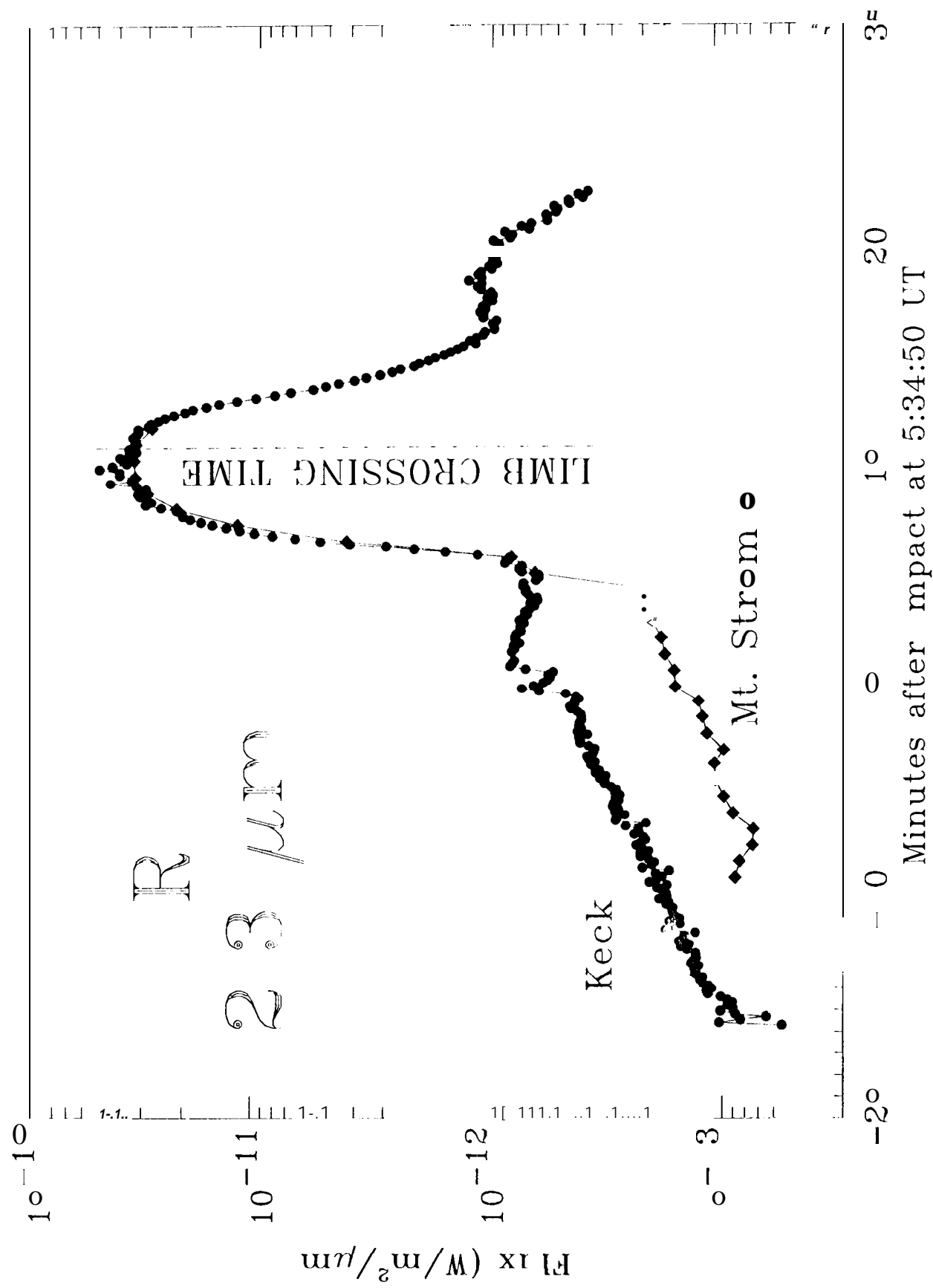


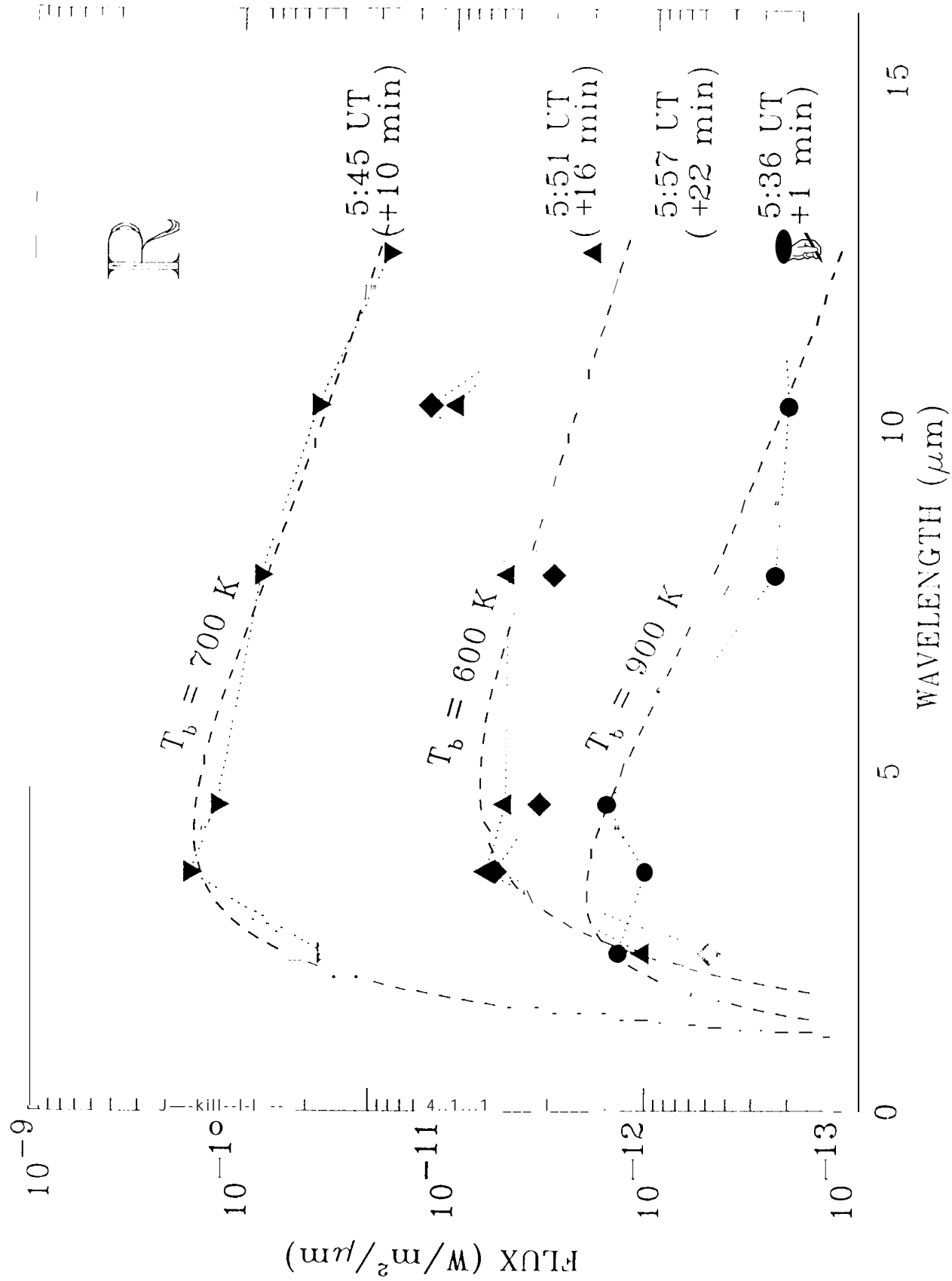


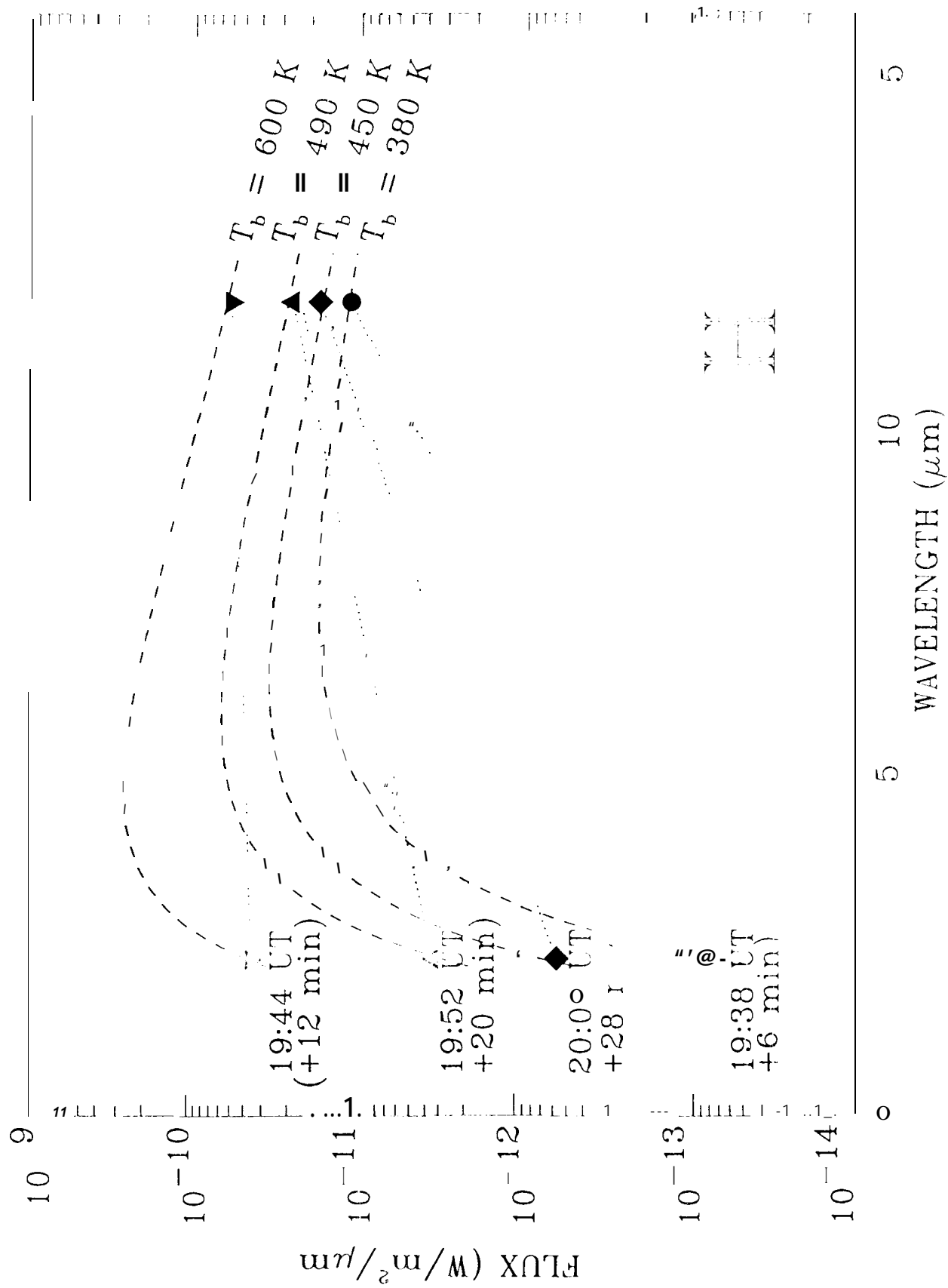


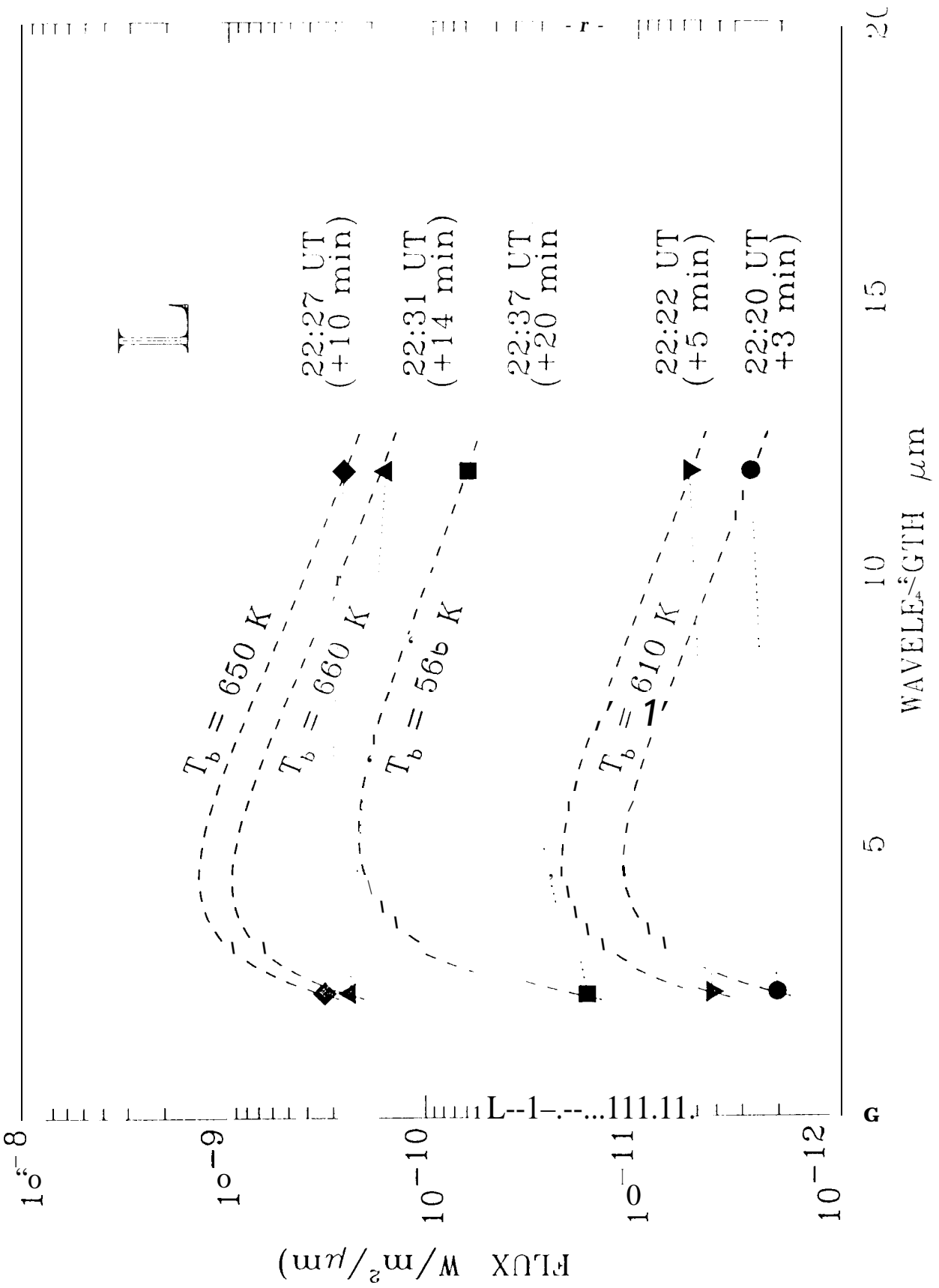












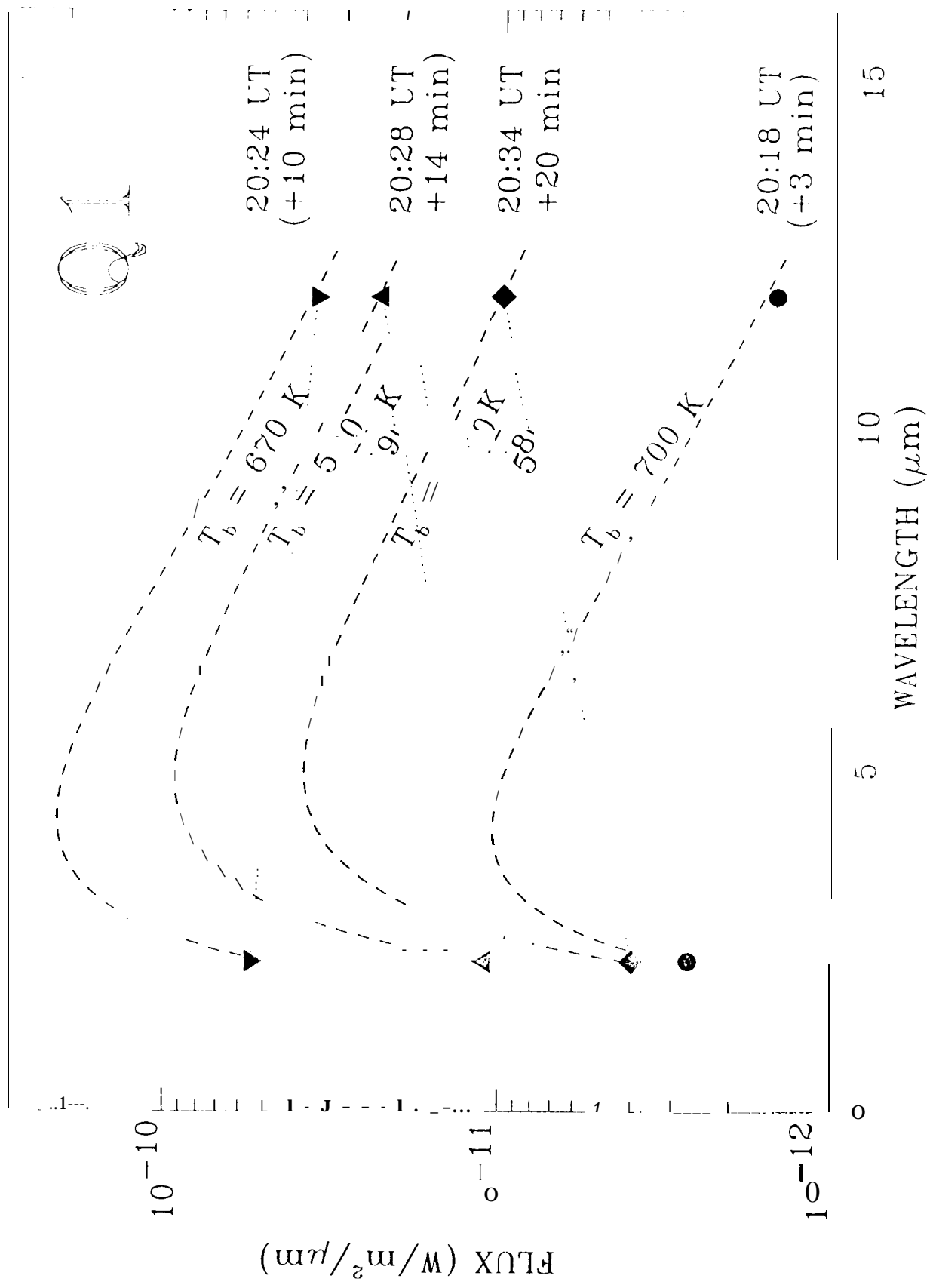


Table 1. Cloud Reflection Parameters

Wavelength	Geometric Albedo
292 nm	0.29
678	0.53
945	0.45
1.84 μm	0.05
2.69	0.20
4.38	0.02

Table 2. Earth-Based Data Corresponding to Galileo-Observed Impacts

Impactor	Instrument	Wavelength
G	Galileo UVS	292 nm
	Galileo NIMS	0.7-5.3 μm
	Galileo PPR	945 nm
	Anglo-Australian Telescope	2-2.5 μm
	Mt. Stromlo	2.3 μm
	SPIREX	2.3 μm
	Keck	3.4 μm
H	HST WF/PC2	555-890 nm
	Swedish Solar Telescope, La Palma	V
	Gregory Coude Telescope	611 nm
	Calar Alto	727 nm, 2.3, 3.1 μm
	IAC-80	750, 892, 950 nm
	Galileo PPR	945 nm
	S. African Astron. Obs.	2.2 μm
	Pic du Midi	2.3 μm
	SPIREX	2.36 μm
	ESO	10 μm
	Nordic Optical Telescope	11.9 μm
K	Galileo SS1	890 nm
	Anglo-Australian Telescope	2-2.5 μm
	Army Surveillance Testbed	2-15 μm (3 than.)
	Okayama Astrophys. Obs.	2.3 μm
	Mt. Stromlo	2.3 μm
	SPIREX	2.36 μm

I.	Gregory Coude Telescope	611 nm
	IAC-80	750,892, 950 nm
	German Solar Vacuum Tower Tel.	890 nm
	Jacobus Kapteyn Tel.	890 nm
	Galileo PPR	945 nm
	Calar Alto	1.2, 2.3 μ m
	Pic du Midi	2.3 μ m
	SPIREX	2.36 μ m
	Palomar	4.5 μ m
	ESO	10 μ m
	Nordic Optical Telescope	11.9 μ m
N	Galileo SS1	890 nm
	Anglo-Australian Telescope	2.3 μ m
Q1	Swedish Solar Telescope, La Palma V	
	Gregory Coude Telescope	611 nm
	Galileo PPR	678, 945 nm
	Calar Alto	727 nm
	IAC-80	750,892, 950 nm
	S. African Astron. Obs.	2.2 μ m
	SPIREX	2.36 μ m
	Nordic Optical Telescope	11.9 μ m
R	Table Mountain obs.	890 nm
	Galileo NIMS	0.7-5.3 μ m
	Anglo-Australian Telescope	2-2.5 μ m
	Mt. Stromlo	2.3 μ m
	McDonald Obs.	2.3 μ m
	Keck	2.3 μ m
	SPIREX	2.36 μ m
	Palomar	3.4, 4.5 μ m
W	HST WF/PC2	555-890 nm
	Galileo SS1	560 nm
	Anglo-Australian Telescope	2-2.5 μ m
	Mt. Stromlo	2.3 μ m

Table 3. Scaling factors for conversion from one point in the spectrum to the integrated blackbody spectrum (μm)

$\lambda, \mu\text{m}$	T: 4 0 0	6 5 0	900 K
2.30	1543.3690	26.316815	6.6722950
3.30	82.075614	7.9095043	4.9027961
4.50	21.145553	6.7779603	6.2187126
7.90	11.189051	12.875135	20.082110
10.3	14.297633	23.747210	42.882729
11.9	18.057005	34.997028	67.179523
12.2	18.910885	37.537665	72.739992

Table 4. Radiative Fallback Energy, erg, assuming emission from a uniform disk

Disk Radius:	Optically thin		Optically thick	
	7°	13°	7°	13°

G impact

Mt. Stromlo at 2.3 μm :

$T_B =$	400 K:	1.82×10^{27}	6.29×10^{27}	1.54×10^{28}	1.39×10^{28}
	650 K:	3.11×10^{25}	1.07×10^{26}	2.63×10^{26}	2.37×10^{26}
	900 K:	7.88×10^{24}	2.72×10^{25}	6.00×10^{25}	6.00×10^{25}

Adopted G Value: 7×10^{25}

H impact

S. Africa at 2.2 μm :

$T_B =$	400 K:	4.67×10^{26}	1.61×10^{27}	5.33×10^{27}	4.93×10^{27}
	650 K:	7.97×10^{24}	2.75×10^{25}	9.09×10^{25}	8.41×10^{25}
	900 K:	2.02×10^{24}	6.97×10^{24}	2.30×10^{25}	2.13×10^{25}

Nordic Optical Telescope at 11.9 μm :

$T_B =$	400 K:	3.56×10^{25}	1.23×10^{26}	2.13×10^{26}	2.00×10^{26}
	650 K:	6.89×10^{25}	2.38×10^{26}	4.12×10^{26}	3.87×10^{26}
	900 K:	1.32×10^{26}	4.56×10^{26}	7.91×10^{26}	7.43×10^{26}

Adopted H Value: 4×10^{25}

K impact

Okayama at 2.3 μm :

$T_B = 400 \text{ K}:$	2.39×10^{27}	8.24×10^{27}	2.59×10^{28}	2.42×10^{28}
650 K:	4.07×10^{25}	1.40×10^{26}	4.42×10^{26}	4.13×10^{26}
900 K:	1.03×10^{25}	3.56×10^{25}	1.12×10^{26}	1.05×10^{26}

Adopted K Value: 9×10^{25}

L impact

Okayama at 2.3 μm , scaled upward by a factor of 2.5:

$T_B = 400 \text{ K}:$	5.97×10^{27}	2.06×10^{28}	6.47×10^{28}	6.06×10^{28}
650 K:	1.02×10^{26}	3.51×10^{26}	1.10×10^{27}	1.03×10^{27}
900 K:	2.58×10^{25}	8.91×10^{25}	2.80×10^{26}	2.62×10^{26}

Nordic Optical Telescope at 11.9 μm :

$T_B = 400 \text{ K}:$	2.09×10^{26}	7.21×10^{26}	7.23×10^{26}	8.70×10^{26}
650 K:	4.05×10^{26}	1.40×10^{27}	1.40×10^{27}	1.69×10^{27}
900 K:	7.77×10^{26}	2.68×10^{27}	2.69×10^{27}	3.24×10^{27}

Adopted L Value: 4×10^{26}

Q1 impact

S. Africa at 2.3 μm :

$T_B = 400 \text{ K}:$	6.87×10^{26}	2.37×10^{27}	8.46×10^{27}	7.79×10^{27}
650 K:	1.17×10^{25}	4.04×10^{25}	1.44×10^{26}	1.33×10^{26}
900 K:	2.97×10^{24}	1.02×10^{25}	3.66×10^{25}	3.37×10^{25}

Nordic Optical Telescope at 11.9 μm :

$T_B = 400 \text{ K}:$	1.83×10^{25}	6.32×10^{25}	1.25×10^{26}	1.13×10^{26}
650 K:	3.55×10^{25}	1.22×10^{26}	2.43×10^{26}	2.19×10^{26}
900 K:	6.81×10^{25}	2.35×10^{26}	4.67×10^{26}	4.20×10^{26}

Adopted Q1 Value: 4×10^{25}

R impact:

Keck 2.2- μm :

$T_B = 400 \text{ K}:$	3.81×10^{26}	1.31×10^{27}	1.52×10^{28}	4.46×10^{27}
650 K:	6.49×10^{24}	2.24×10^{25}	2.59×10^{26}	7.95×10^{25}
900 K:	1.65×10^{24}	5.68×10^{24}	6.57×10^{25}	2.02×10^{25}

Palomar, 3.4-μm:

$T_B = 400 \text{ K}:$	8.58×10^{25}	2.96×10^{26}	1.08×10^{27}	9.86×10^{26}
650 K:	8.27×10^{24}	2.85×10^{25}	1.04×10^{26}	9.50×10^{25}
900 K:	5.13×10^{24}	1.77×10^{25}	6.48×10^{25}	5.89×10^{25}

Palomar, 4.5-μm:

$T_B = 400 \text{ K}:$	1.56×10^{25}	5.37×10^{25}	1.39×10^{26}	1.85×10^{26}
650 K:	4.99×10^{24}	1.72×10^{25}	4.44×10^{25}	5.93×10^{25}
900 K:	4.58×10^{24}	1.58×10^{25}	4.08×10^{25}	5.44×10^{25}

IRTF, 7.85-μm:

$T_B = 400 \text{ K}:$	1.23×10^{24}	4.24×10^{24}	1.23×10^{25}	1.11×10^{25}
650 K:	1.41×10^{24}	4.88×10^{24}	1.41×10^{25}	1.28×10^{25}
900 K:	2.21×10^{24}	7.61×10^{24}	2.20×10^{25}	2.00×10^{25}

IRTF, 10.3-μm:

$T_B = 400 \text{ K}:$	2.01×10^{24}	6.94×10^{24}	1.38×10^{25}	1.32×10^{25}
650 K:	3.34×10^{24}	1.15×10^{25}	2.30×10^{25}	2.19×10^{25}
900 K:	6.03×10^{24}	2.08×10^{25}	4.15×10^{25}	3.95×10^{25}

IRTF, 12.5-μm:

$T_B = 400 \text{ K}:$	1.57×10^{24}	5.43×10^{24}	1.06×10^{25}	9.94×10^{24}
650 K:	3.29×10^{24}	1.13×10^{25}	2.22×10^{25}	2.08×10^{25}
900 K:	6.06×10^{24}	2.09×10^{25}	4.08×10^{25}	3.82×10^{25}

Adopted R Value: 1×10^{25}

Note: Adopted values are uncertain by a factor of -10.